INTEGRATION OF CFD MODELLING AND UAV PHOTOGRAMMETRY FOR DAMAGE PROGRESSION ASSESSMENT OF A RUBBLE MOUND BREAKWATER

Elisa Leone[1], Antonio Francone[1], Agostino Lauria[1], Andrea Paglialunga[2], Felice D'Alessandro[3], Giuseppe Roberto Tomasicchio[1]

Rubble-mound breakwaters are structures specifically designed to protect coastal areas from wave action requiring robust design and ongoing monitoring to maintain their structural integrity. The study presents an experimental and numerical investigation of damage progression in a small-scale model of a rubble-mound breakwater, conducted at the EUMER laboratory. The physical model, featuring Accropode© II and Accroberm© I armour units, has been subjected to storm-like conditions, and the progression of damage has been assessed using an innovative UAV photogrammetry approach. The proposed method enabled the evaluation of areas where erosion and accretion occur due to the action of extreme waves, identifying critical zones most susceptible to damage. To complement the experimental findings, a numerical simulation using OpenFOAM libraries combined with OlaFlow, a Computational Fluid Dynamics (CFD) model, has been integrated using the observed data. The CFD model provided additional insights into the flow fields and forces distributions acting on the structure, contributing a more detailed understanding of the damage mechanisms. The combination of UAV photogrammetry and CFD analysis allowed for a deeper assessment of the damage evolution, offering a comprehensive approach to breakwater design and maintenance strategies.

Keywords: rubble-mound breakwater; porous structures; UAV photogrammetry; CFD modelling

INTRODUCTION

Rubble mound breakwaters are designed to dissipate wave energy and protect coastlines and ports. Among the various armor units developed over time, Accropode© II, introduced in 2000s, is engineered for a strong interlocking system that enhances its initial stability through a high packing density (Giraudel et al., 2014). However, once damage initiates, the progression can be rapid, as even the removal of a single unit leads to a significant reduction in packing density and increased vulnerability to damage. Understanding what happens after the stability limit is reached and the speed of damage evolution is crucial for maintenance and repair purposes.

Several experimental studies have explored the damage progression of rubble-mound breakwaters under wave forces, revealing critical vulnerabilities in different sections of the structure (Hofland et al., 2014; Comola et al., 2014; Sande et al., 2016). Modern monitoring technologies, such as UAV photogrammetry, laser scanning, and 3D imaging techniques, have significantly advanced damage assessment by providing detailed insights into erosion and material displacement over time (Puente et al., 2014; Musumeci et al., 2018; Lemos et al., 2022; Marino et al., 2023).

The present paper introduces a practical image-based approach for monitoring breakwater damage progression. An experimental investigation has been conducted at the EUMER (EUropean Maritime Environmental Research) lab, in Italy, on a down-scaled breakwater featuring Accropode© II and Accroberm© I armour units to assess damage progression over time. The resulting erosion and accretion maps highlight critical zones of material loss and accumulation.

Additionally, the study integrates a CFD numerical analysis to simulate the forces acting on the breakwater. The adopted numerical model is OlaFlow which utilizes OpenFOAM libraries, that allows the generation and absorption of wave conditions as boundary conditions and allows simulation of flow within porous media. The numerical model provided additional information on pressure distributions and wave forces acting on the rubble mound surface, offering insights into wave-structure interactions and enhancing the understanding of the physical processes governing breakwater stability and failure mechanisms. The importance of detailed flow field and pressure distribution data is well-established in the literature, as it plays a crucial role in advancing the knowledge and predictive capabilities related to breakwater performance under wave action (Brunone and Tomasicchio, 1997; Mahmoudi Kurdistani et al., 2021).

[1] Department of Engineering for Innovation, University of Salento, Lecce, Italy
[2] eCampus Telematic University, Novedrate, Italy
[3] Department of Environmental Science and Policy, University of Milan, Milan, Italy

EXPERIMENTAL INVESTIGATION

The experimental investigation has been carried out at the EUMER laboratory (www.eumer.eu), located at the University of Salento in Lecce, Italy. The physical model has been built in the 3D wave basin measuring 29.5 m in length, 28 m in width, and 1.6 m in depth. The wave generation is performed using a piston-type system comprising 56 independently controlled paddles, able to produce both unidirectional and directional wave fields, including regular waves and wave spectra. The wave generation system includes an active wave absorption feature designed to eliminate unwanted reflected wave energy.

A physical model of the rubble-mound breakwater at the Port of Arenella in Sicily, Italy, has been constructed at a 1:40.8 scale and tested in a wave basin to investigate its hydraulic performance under extreme wave conditions. It consists of a core, underlayer and toe composed of rocks of various sizes and weights and an armour layer composed of a single layer of Accropode© II units supported by a single row of Accroberm© I units. The Accropode© II armour units have been interlocked following the guidelines provided by the manufacturing company CLI (Concrete Layer Innovative). The down-scaled physical model is divided into distinct areas: the port side, the roundhead and the trunk, with a slope of 2/3. The model also includes a transition to a different armor layer composed of cubic armor units.

Two categories of armor units have been used, varying in weight and size: smaller units (Cat.7) on the trunk and larger units (Cat.8) on the roundhead. The transition between these unit categories, as well as the transition between Accropode© II and cubic armour units, have been carefully executed for optimal alignment and support. Figure 1 shows a top view of the constructed model in the wave basin: the different areas of the physical model are highlighted in blue while the types and categories of the armor units used are marked in yellow.

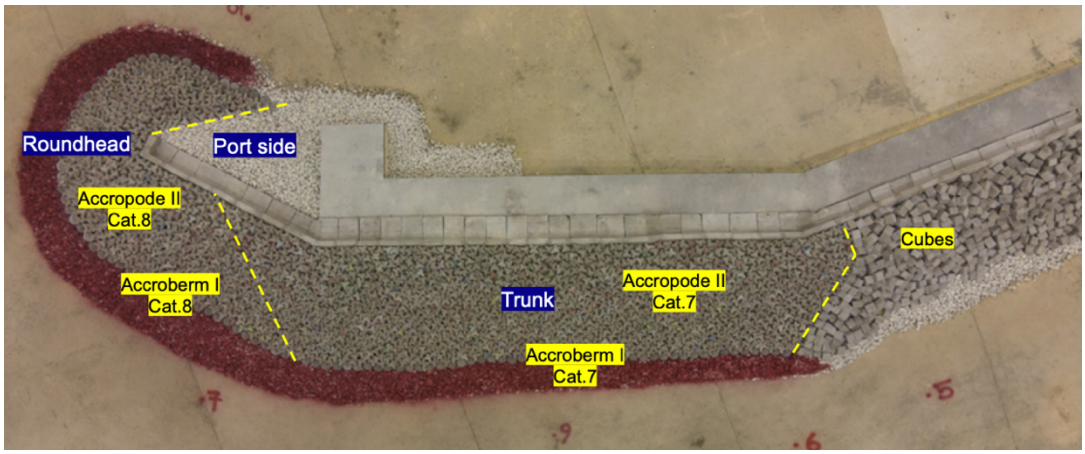

Figure 1. Top view of the complete physical model in the wave basin

Table 1 provides the range of median diameter, D_{n50}, and weight, M, of each rock category in model scale and the volume, V, and weight, M, of the armour units in model scale.

Table 1. Characteristics of the rock materials and armour units in model scale

Layer	D_{n50} (cm)	M (g)
Core	0.3 – 1.8	0.1 – 16.1
Under Layer	1.8 – 2.3	16.0 – 31.6
Armour Layer (port side)	2.0 – 2.4	19.5 – 34.4
Toe	1.6 – 2.1	11.5 – 22.9
Armour unit	**V (cm^3)**	**M (g)**
Accropode© II Cat. 7	87.7	205.3
Accroberm© I Cat. 7	89.4	205.5
Accropode© II Cat. 8	116.4	273.0
Accroberm© I Cat. 8	118.0	271.2

In the present study, the results of a single wave attack are presented, corresponding to an irregular wave scenario that represents a potential extreme event, aimed at simulating a complete failure of the small-scale breakwater. The wave height, H_s, and peak period, T_p, have been set at 0.197 m and 1.96 s, respectively, at a direction of 20 degrees to the orthogonal axis of the wave generator and with a water level, h, of 0.286 m at the armor layer toe in model scale. Wave data have been collected using four wave gauges (WG1-4) located upstream from the structure, allowing the separation between incident and reflected wave conditions from the structure. The reflection analysis has been conducted using the method developed by Mansard and Funke (1980) and later extended by Zelt and Skjelbreia (1993).

The wave attack has been replicated five times, with a variable number of waves (550, 550, 1049, 2047 and 2047 waves, respectively), leading to a cumulative total of 6243 reproduced waves. After each step, the wave basin has been drained and a survey of the entire structure has been performed using a UAV equipped with a high-resolution camera. Table 2 summarizes the sequence of wave steps, including the duration, t, the number of waves, N_w, cumulative duration, t_{cum} and the cumulative wave count, $N_{w,cum}$.

Table 2. Wave steps with duration, number of waves and the cumulative count of waves.

Wave step	t (s)	N_w (-)	t_{cum} (s)	$N_{w,cum}$ (-)
1	1078	550	1078	550
2	1078	550	2156	1100
3	2056	1049	4212	2149
4	4012	2047	8224	4196
5	4012	2047	12236	6243

IMAGE PROCESSING

On the small-scaled physical model, a number of markers have been strategically positioned to aid in spatial orientation. High-resolution images have been captured using UAV technology before and after model construction, as well as after each wave step. Through a process of image alignment and camera parameter calibration, the images have been used to reconstruct point clouds containing three-dimensional spatial information. The resulting point clouds have been imported into *CloudCompare*, an open-source software for visualizing, comparing, and analyzing spatial data.

The image analysis has been confined on the model's footprint, divided into 10 sectors: port-side (sector 1), roundhead (sectors 2-5), trunk (sectors 6-9), and transition area (sector 10). Figure 2 shows the model footprint before and after construction, which will be referred to as the "as-built" model hereinafter.

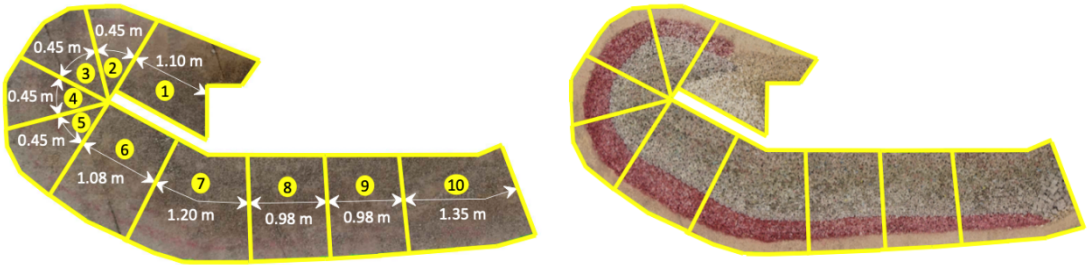

Figure 2. Model footprint with designated sectors used for image analysis: before (left panel) and after (right panel) model construction

Sector 6 presents the transition zone with an equal distribution of 50% between cat.8 and cat.7 armour units, while sector 10 presents the transition from cat.7 units to cubic armor units.

The comparison of pre- and post-construction point clouds in *CloudCompare* allowed to obtain the initial sector volumes by summing the volumes of basic parallelepipeds. These parallelepipeds are formed using the height difference (z-coordinates) between corresponding points in the two clouds, meaning between points in the pre- and post-construction clouds.

An initial calibration has been carried out to find the optimal grid size for volume calculation, concluding at a cell size of 1 mm. To handle empty cells within point clouds, interpolation of neighboring data has been used. The volume calculation has been repeated after each wave step. Figure 3 shows the point clouds of sector 3 as built and after wave steps 1-5.

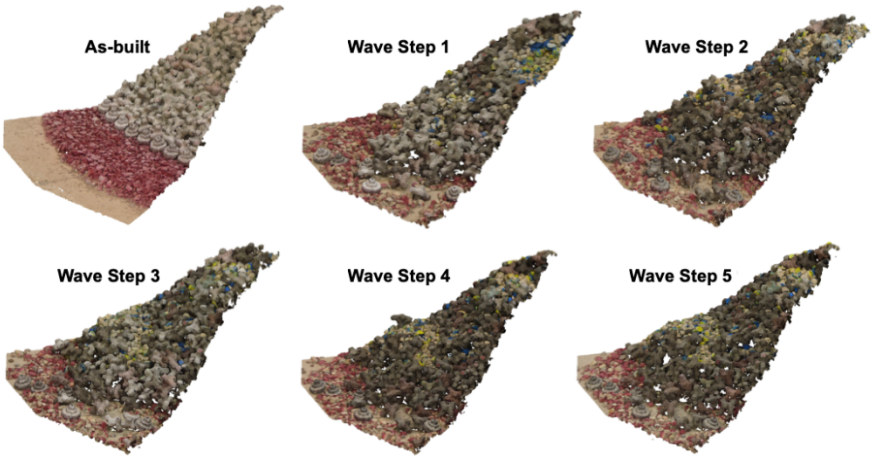

Figure 3. Point clouds as-built and after wave steps 1-5 of sector 3

Damage progression assessment

The UAV surveys and point clouds analysis provided a comprehensive view of erosion and accretion patterns across the entire physical model. Figure 4 shows the damage progression over time for wave steps 1-5 across sectors 1-10. The figure is organized into two columns: the right one showing overhead point clouds after each wave step, and the left one highlighting erosion (in red) and accretion (in blue). Within the wave step 1 a significant material displacement in sectors 1 (port side) and 3 (roundhead) can be observed. Within steps 2 and 3, further displacement in the roundhead can be noted, extending to sectors 4 and 5 with erosion on the upper and accumulation on the lower sides. By wave step 3, sector 10 (transition zone with cubic units) showed a significant material displacement, marking it as a critical zone, yet still presenting a balance between erosion and accretion. As testing advanced, within wave steps 4 and 5, displacement spread from sector 10 to the trunk (sectors 6-9) and roundhead. By wave step 5, erosion impacted not just the armor layer but reached the underlayer in scattered areas of the model, eventually exposing the core.

Figure 5 summarizes the erosion and accretion evolution with respect to wave count for sectors 1-10. The x-axis represents the wave count and the y-axis indicates the percentage of eroded (left panel) and accreted (right panel) volumes relative to initial volumes. Sector 10 experienced the highest erosion, affecting about 50% of material, particularly after the 1100th wave, while sectors 9, 8, and 7 showed a gradual increase in erosion. The roundhead, however, showed early but limited erosion, peaking at 10% in sector 5 by the 550th wave.

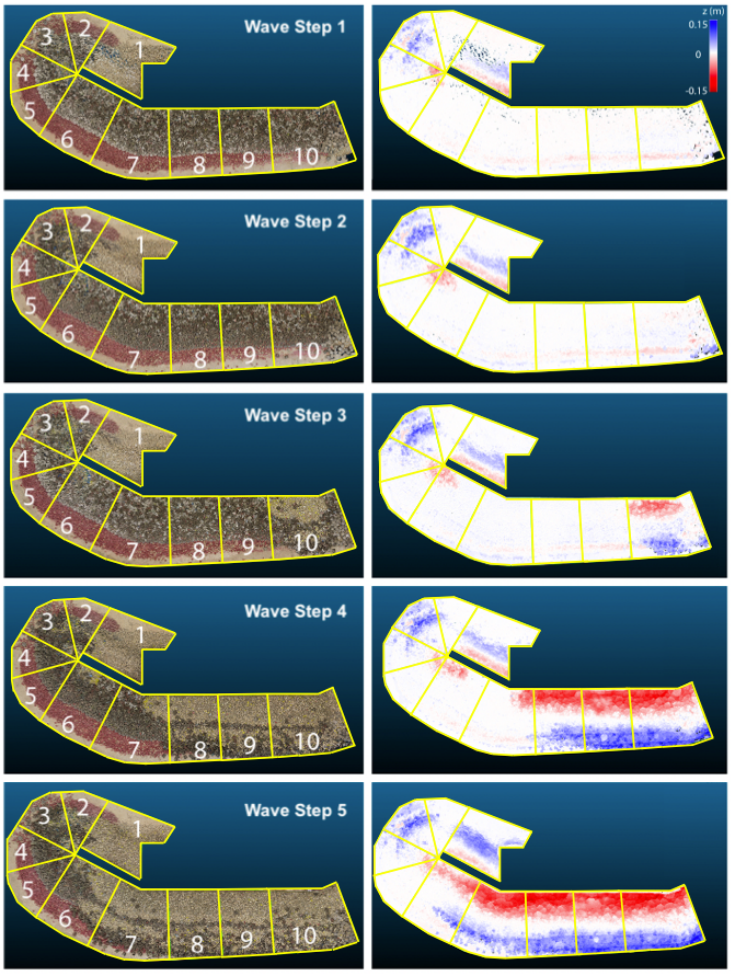

Figure 4: Damage progression maps for wave steps 1-5 on sectors 1-10

For accretion, similar to erosion, sector 10 showed the highest impact, followed by sectors 9, 8, and 7. Behind the port, accretion was notable, likely due to displaced material from the trunk, particularly sector 6, where erosion was significant. Accumulation in sectors 10 and 9 increased until wave 4196, after which it stabilized, while sector 3 reached stability by wave 2149. The discrepancy between eroded volume (50% in sector 10) and accumulated volume (20% in the same sector) suggests that numerous armor units shifted beyond the model's boundaries.

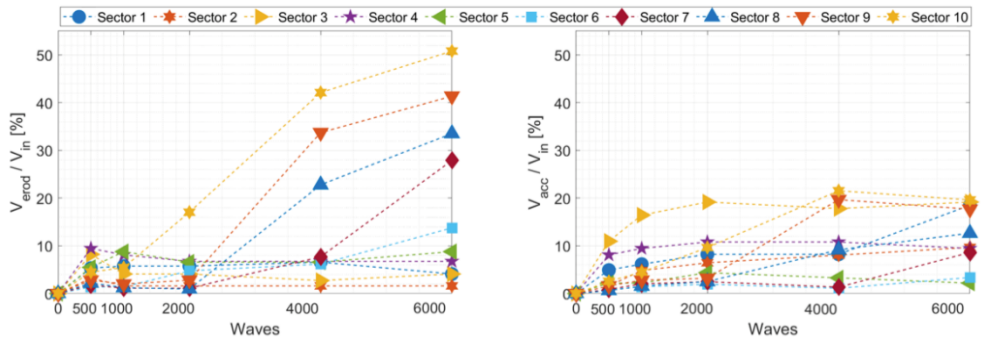

Figure 5: Percentage variation of volumes in terms of erosion (left panel) and accumulation (right panel) in relation to the wave count for sectors 1-10

NUMERICAL MODEL

The surveys of the bathymetry and the physical model in the "as-built" configuration have been subsequently used to numerically replicate the wave conditions tested in the laboratory, using the CFD solver OlaFlow based on the OpenFOAM libraries. The numerical study has been carried out using a three-dimensional grid. The full numerical domain has been designed in order to capture a broad range of hydrodynamic phenomena and their effects on the structure. The domain has been set to 13 m in width and 13 m in length with a depth of 1 m and has been oriented to ensure that waves impact the structure perpendicularly, avoiding the generation of oblique waves, facilitating numerical calculations.

Static boundaries have been implemented for wave generation on one edge of the domain and for wave absorption on the opposite edge (Higuera et al., 2013). Wave generation has been simulated by applying the free surface elevation over time observed experimentally at WG1. Wave absorption has been modeled by incorporating the reflection coefficient observed experimentally in the basin without the constructed model, to replicate real conditions in a confined environment. The volume of fluid (VOF) method has been used to track the free-surface by capturing the interface between two immiscible fluids (in this case air and water) within the computational domain (Hirt and Nichols, 1981). The free surface has been defined using the variable *alpha.water*, which represents the water volume fraction in each computational cell. The edges of the domain parallel to the wave direction and the bathymetry have been considered as walls, where the velocity has been set to zero. The structure has been defined as a porous medium with a uniform porosity of 0.4 which represents a commonly used value to simulate coastal structures (Higuera et al., 2014). The decision to use a single value of porosity stems from the fact that the UAV survey has been conducted after the structure was fully constructed, which prevented distinguishing and assigning different porosity values to individual layers. The boundary conditions used in the simulation are summarized in Table 3. Figure 6 shows the numerical domain indicating the location of the boundary conditions and the porous structure. The simulations were carried out using 8 processors through the public domain open MPI implementation of the standard message passing interface (MPI) for parallel running on a CPU-based computational system.

Table 3. Boundary conditions in the numerical model.

Boundary	BC for alpha.water	BC for velocity	BC for pressure
Inlet	waveAlpha	waveVelocity	fixedFluxPressure
Outlet	zeroGradient	waveAbsorption2DVelocity	fixedFluxPressure
Side walls	Symmetry	Symmetry	Symmetry
Bottom	zeroGradient	fixedValue (0)	fixedFluxPressure
Atmosphere	inletOutlet	pressureInletOutletVelocity	totalPressure

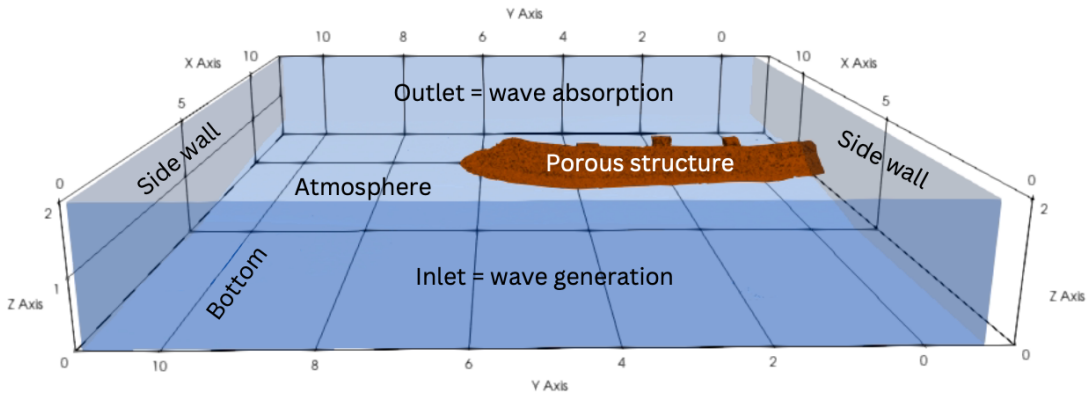

Figure 6. 3D view of the numerical domain

OpenFOAM uses the finite volume method to solve the Navier-Stokes (NS) equations, an Eulerian approach that evaluates fluxes through fixed control volumes. A transient Reynolds-Averaged Navier-

Stokes (RANS) method has been applied in the present work, using conventional RANS equations for incompressible fluids, commonly employed in coastal engineering. The governing equations consist of the mass conservation equation:

$$\frac{\partial \rho}{\partial t} + \nabla \cdot (\rho \overline{\boldsymbol{U}}) = 0 \tag{1}$$

and the momentum equation:

$$\frac{\partial}{\partial t}(\rho \overline{\boldsymbol{U}}) + \nabla \cdot (\rho \overline{\boldsymbol{U}}\overline{\boldsymbol{U}}) = -\nabla \bar{p} + \rho \boldsymbol{g} + \nabla \cdot (\mu \nabla \overline{\boldsymbol{U}} + \tau) \tag{2}$$

where $\overline{\boldsymbol{U}}$ is the average fluid velocity vector accounting for three components for three-dimensional cases, ρ is the fluid density, $\bar{p}$ is the average dynamic pressure (the difference of the total pressure and the hydrostatic pressure), $\boldsymbol{g}$ is the gravitational acceleration vector, μ is the dynamic viscosity of the fluid and τ is the Reynolds stress tensor.

In OlaFlow, porous media are modeled using a macroscopic approach that calculates the average pressure loss within the medium. This requires modifying the standard RANS momentum equation in VARANS (Volume-Averaged Reynolds-Averaged Navier-Stokes) momentum equation to account for pressure loss and the limited amount of fluid (Hsu et al. 2002). The pressure loss is represented by a hydraulic gradient, *I*, which is defined as the pressure change per unit length, Δx. Based on the works of Darcy (1856), Forchheimer (1901), and Polubarinova-Koch (2015), the hydraulic gradient is described by the extended Forchheimer equation:

$$I = \frac{\Delta P}{\Delta x} = Au + Bu|u| + C\rho \frac{\partial u}{\partial t} \tag{3}$$

where u is the pore velocity, A (linear term) is the hydraulic gradient under laminar flow conditions, where inertial forces are negligible, B (quadratic term) accounts for the effects of turbulent flow and C (time-dependent term) represents the acceleration of the fluid through the porous medium. Together, the first two terms account for the drag forces, while the third term corresponds to the inertial forces. Following Engelund's definition (1953), later modified by Van Gent (1996), the coefficients are expressed as:

$$A = \alpha \frac{(1-n)^3}{n^2} \frac{\mu}{D_{50}^2} \tag{4}$$

$$B = \beta \left(1 + \frac{7.5}{KC}\right) \frac{1-n}{n^3} \frac{\rho}{D_{50}} \tag{5}$$

$$C = \frac{c}{\Delta x} \tag{6}$$

where n is the porosity, defined as the ratio between the pore volume and the total volume, ν is the kinematic viscosity of the fluid, D_{n50} is the mean grain diameter of the porous medium and KC is the Keulegan–Carpenter number. α, β, and are coefficients that need to be calibrated for different types of porous media, and, based on prior research, the value of c = 0.34 is commonly considered (del Jesus et al., 2012). k-omega SST model has been used as the turbulence closure model (Menter, 1994). This model has been already used in several different flow cases, always giving satisfactory results (see, among others, Lazzaro et al. 2024).

Model calibration

The calibration process involved optimizing the mesh resolution and determining the linear and non-linear flow resistance coefficients for the porous medium. The results of the calibration process are directly linked to the free surface elevation over time calculated by the numerical model close to the wave generation boundary and compared with the experimental observations at WG1. If the numerical output deviates significantly, the parameters are adjusted iteratively until satisfactory agreement is achieved.

As a result of the calibration process, the numerical domain has been vertically divided into three blocks, each with varying mesh resolutions tailored to specific simulation requirements. A finer mesh has been applied in the lowest block to accurately capture the interaction between water and the bathymetry. A slightly coarser mesh has been used in the middle block, corresponding to the free water surface, to effectively simulate wave-structure interactions. Finally, an even coarser mesh has been employed in the top block to complete the domain. Table 4 lists the grid resolution of the three blocks in all directions (x,y,z).

Table 4. Grid resolution for different blocks

Block	Grid size Δx x Δy x Δz [m]
Block 1	0.05 x 0.05 x 0.010
Block 2	0.05 x 0.05 x 0.015
Block 3	0.05 x 0.05 x 0.020

The flow resistance coefficients have been calibrated as follows: $\alpha = 0$, $\beta = 2$ (consistent with Lin, 1998, under similar conditions), and $c = 0.34$ (a commonly used value, as suggested by del Jesus, 2012). In the clear fluid region, all coefficients (α, β and c) have been set to zero, as no porous medium effects are present there.

Figure 7 shows a comparison between the experimentally observed and numerically simulated free surface elevation at the wave generation boundary, as a result of model calibration. The plot displays data over a restricted time interval, 40 s, to better visualize the comparison between experimental and numerical results. The agreement is generally good, although the numerical model slightly underestimates the experimental results. However, these deviations remain within acceptable tolerance limits, demonstrating the effectiveness of the calibration process.

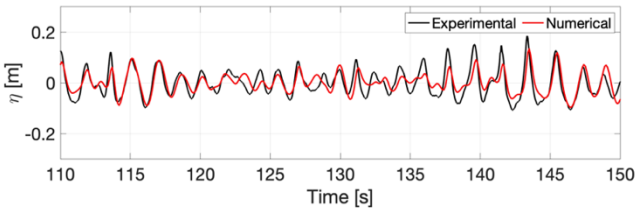

Figure 7: Comparison between the experimental and numerical free surface elevation at the wave generation boundary

Wave forces distribution

The numerical setup, calibrated in terms of mesh resolution and linear and non-linear flow resistance coefficients, has been employed to simulate the experimental test conducted in the laboratory.

The duration of the numerical simulation has been set to match the duration of wave step 1 from the experimental laboratory test. This approach was chosen to focus solely on assessing the pressure field and the forces acting on the structure. The numerically estimated pressure field at the surface of the breakwater have been used to determine the distribution of the acting forces on the structure. The forces have been evaluated considering the pressure over each cell, based on the local resolution.

Figure 8 shows contour plots of the force components estimated numerically in both perpendicular, $F_{x,}$ and parallel, F_y, direction respect to the surface of the structure. The force components have been presented in dimensionless form with respect to their maximum values. Positive forces are shown in red, while negative forces are depicted in blue. The three plots in the figure represent three distinct time steps: the top panel illustrates the moment when a wave begins to impact the structure, while the subsequent panels depict later instances, each separated by a time interval of 0.5 seconds.
As expected, F_x exhibit positive values on the front face of the structure and negative values on its rear side, with their intensity varying with depth. F_y also vary with depth and exhibit significant values in critical areas where damage has been observed experimentally within wave step 1. Specifically, intense values are detected on the port side (see squared dotted boxes in the figure 8), intense values are observed at the roundhead (see squared solid boxes in the figure 8), and intense values are noticeable in the transition zone with the cube armour units (see circles in the figure 8).

The numerical model supported the experimental findings by demonstrating that the critical areas with higher force values corresponded to those that experimentally proven to be critical and ultimately led to structural failure in subsequent wave steps.

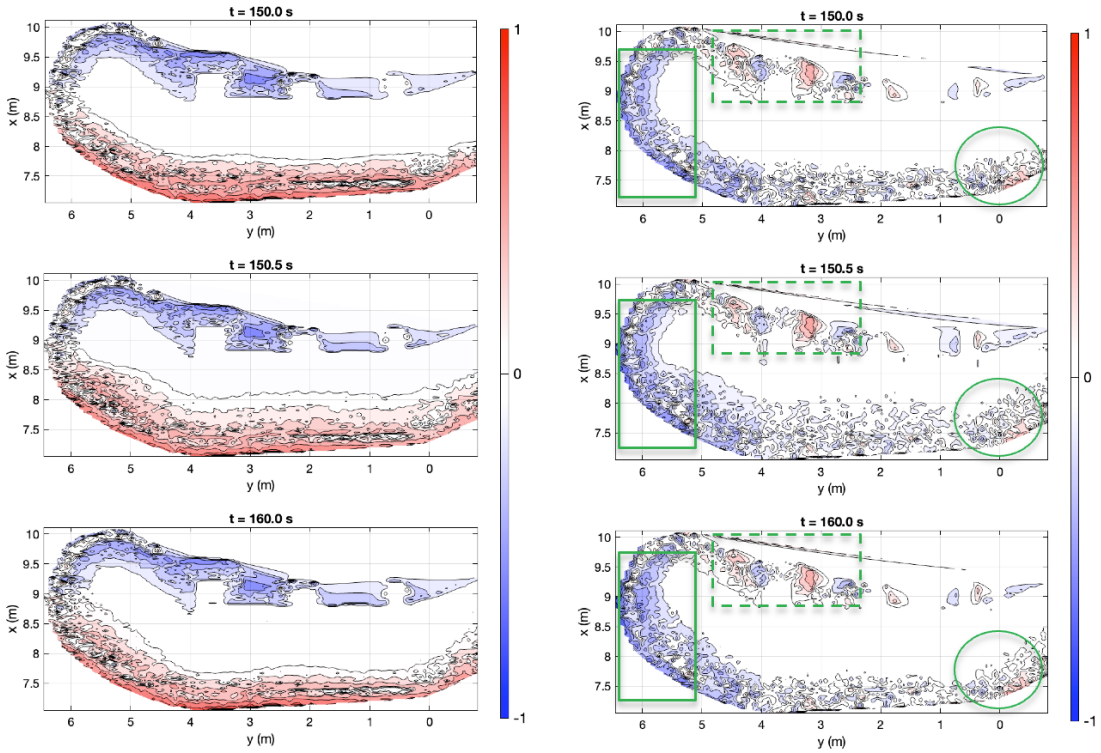

Figure 8: Perpendicular dimensionless component of force, F_x, (left panel) and parallel dimensionless component of force, F_y, (right panel)

CONCLUSIONS

Monitoring rubble-mound breakwaters is essential to ensure stability and safety over time. Understanding failure mechanisms, even beyond the failure limit, supports effective, rapid maintenance. Modern tools allow early detection of deterioration, enabling quick intervention, especially useful in laboratory settings where design solutions are tested. The present study aimed to enhance the understanding of breakwater damage progression by combining image-based techniques with CFD modeling.

Laboratory experiments at the EUMER lab have been conducted to analyze damage in a down-scaled rubble mound breakwater model with Accropode© II armor and Accroberm© I toe units, tested under extreme wave conditions for 6243 cumulative waves across five tests. After each test, UAV-based aerial surveys provided data for detailed erosion and accretion maps through point cloud volume calculations.

On the port side, material displacement has been evident from 550 waves, with significant accumulation between 4196 and 6243 waves, reaching 5% erosion and 20% accretion by the end. At the roundhead, erosion has been widespread early on (up to 10% in sectors 4 and 5 within 1100 waves) while accumulation peaked at 20% in sector 3 after 2149 waves. In the transition zone, progressive erosion spread from sector 10 to 6, with sector 10 experiencing up to 50% erosion and 20% accretion by 6243 waves, pushing some armor units beyond the assessment domain.

Then, the numerical model OlaFlow, which utilizes OpenFOAM libraries, has been calibrated and adopted based on experimental data to assess its effectiveness in identifying the critical areas of the structure that experienced higher stresses in terms of forces acting on the structure. The numerical model qualitatively supported the experimental findings, demonstrating that the critical areas with higher values of forces corresponded to those that experimentally showed a predisposition to damage. These areas served as the initial points from which the damage subsequently spread.

The study demonstrates the practical value of an image-based approach for tracking damage progression in laboratory environments. Moreover, the integration of UAV technology and CFD modeling in this research paves the way for its broader application in future coastal engineering studies, enhancing our understanding of structural vulnerabilities and potential improvements.

ACKNOWLEDGMENTS

The present research was funded by the European Union – Next Generation EU through the grant of the project PRIN 2022 titled “NonlinEar Phenomena in floaTing offshore wind tUrbiNEs (NEPTUNE)”, Project code: 2022W7SKTL.

REFERENCES

Brunone, B. and Tomasicchio, G.R. (1997). Wave kinematics at steep slopes: second order model. *Journal of Waterway, Port, Coastal and Ocean Eng*., ASCE, 123, 5, pp. 223–232.

Comola, F., Andersen, T. L., Martinelli, L., Burcharth, H. F. and Ruol, P. (2014). Damage pattern and damage progression on breakwater roundheads under multidirectional waves. *Coastal engineering*, 83:24–35.

Darcy, H. (1856). Les Fontaines Publiques de la Ville de Dijon (The Public Fountains of the City of Dijon). Dalmont: Paris, France

del Jesus, M., Lara, J.L. and Losada, I.J. (2012). Three-dimensional interaction of waves and porous coastal structures: Part I: Numerical model formulation. *Coastal Engineering*, *64*, pp.57-72.

Engelund, F. (1953). On the Laminar and Turbulent Flows of Ground Water through Homogeneous Sand; Technical Report, *Danish Academy of Technical Sciences*

Forcheimer, P. (1901). Wasserbewegung durch Boden. *Zeitschrift des Vereines Deutscher Ingenieure*., 45, no. 50: 1781-1788.

Giraudel, C., Garcia, N., and Ledoux, S. (2014). Single-layer breakwater armouring: Feedback on the accropode technology from site experience. *Coastal engineering*, pp.1-15.

Higuera, P., Lara, J.L. and Losada, I.J. (2013). Realistic wave generation and active wave absorption for Navier–Stokes models: Application to OpenFOAM®. *Coastal Engineering*, *71*, pp.102-118.

Higuera, P., Lara, J.L. and Losada, I.J. (2014). Three-dimensional interaction of waves and porous coastal structures using OpenFOAM®. Part II: Application. *Coastal Engineering*, *83*, pp.259-270.

Hirt, C.W. and Nichols, B.D. (1981). Volume of fluid (VOF) method for the dynamics of free boundaries. *J. Comput. Phys*. 39 (1), 201–225.

Hofland, B., Disco, M., and Van Gent, M. (2014). Damage characterization of rubble mound roundheads. *Proc. CoastLab2014*. Varna, Bulgaria.

Hsu, T.J., Sakakiyama, T. and Liu, P.L.F. (2002). A numerical model for wave motions and turbulence flows in front of a composite breakwater. *Coast. Eng.* 46, 25–50. [CrossRef]

Lazzaro, E., Francone, A., Leone, E., Lauria, A., Barbaro, G., Tomasicchio, G.R. (2024). Experimental and Numerical Efficiency Analysis of Absorbing-Type Vertical Breakwater *International Symposium: New Metropolitan Perspectives*, 336-344

Lemos, R., Santos, J. A., and Fortes, C. J. (2022). Damage evolution prediction during 2d scale-model tests of a rubble-mound breakwater: A case study of Ericeira's breakwater. *Modelling*, 4(1):1–18.

Lin, P. and Liu, P.-F. (1999). Internal wave-maker for Navier–Stokes equations models. *Journal of Waterway, Port, Coastal, and Ocean Engineering*, 125:207–215.

Liu, P.-F., Lin, P., Chang, K., and Sakakiyama, T. (1999). Numerical modeling of wave interaction with porous structures. *Journal of Waterway, Port, Coastal, and Ocean Engineering*, 125:322–330.

Mahmoudi Kurdistani, S., Aristodemo, F., Francone, A., Tripepi, G. and Tomasicchio, G. R. (2021). Formula for the maximum reference pressure at the interface of the breakwater core and filter layer. *Coastal Engineering*, 63(4), 532-544.

Mansard, E. P. and Funke, E. (1980). The measurement of incident and reflected spectra using a least squares method. *Coastal Engineering*, pp 154–172.

Marino, S., Galantucci, R. A., and Saponieri, A. (2023). Measuring rock slope damage on rubble mound breakwater through digital photogrammetry. *Measurement*, 211:112656.

Menter, F.R. (1994). Two-equation eddy-viscosity turbulence models for engineering applications. *AIAA journal*, 32(8), pp.1598-1605.

Musumeci, R.E., Moltisanti, D., Foti, E., Battiato, S. and Farinella, G.M., (2018). 3-D monitoring of rubble mound breakwater damages. *Measurement*, 117, pp.347-364.

Polubarinova-Kochina, P.YA. (1962). Theory of ground water movement. *Princeton University Press*. 613-pp.

Puente, I., Sande, J., González-Jorge, H., Peña-González, E., Maciñeira, E., Martínez-Sánchez, J. and Arias, P. (2014). Novel image analysis approach to the terrestrial lidar monitoring of damage in rubble mound breakwaters. *Ocean engineering*, 91:273–280.

Sande, J., Peña, E., and Maciñeira, E. (2016). Damage criteria in roundheads armoured with a single layer of cubipod armor units. *Coastal Engineering Proceedings*, (35):13–13.

Van Gent, M.R.A. (1996). Wave interaction with permeable coastal structures. In *International Journal of Rock Mechanics and Mining Sciences and Geomechanics Abstracts* (Vol. 6, No. 33, p. 277A).

VandenBosch, A., Angremond, K.D., Jan Verhagen, H. and Olthof, J. (2003). Influence of the density of placement on the stability of armour layers on breakwaters. In *Coastal Engineering 2002: Solving Coastal Conundrums* (pp. 1537-1549).

Whitaker, S. (1996). The Forchheimer equation: a theoretical development. *Transport in Porous media*, *25*(1), pp.27-61.

Zelt, J. and Skjelbreia, J. E. (1993). Estimating incident and reflected wave fields using an arbitrary number of wave gauges. In *Coastal Engineering* 1992, pages 777–789.